Monthly Notices
of the
ROYAL ASTRONOMICAL SOCIETY

Mon. Not. R. Astron. Soc. **427,** 1651–1665 (2012) doi:10.1111/j.1365-2966.2012.22080.x

Constraining extended gamma-ray emission from galaxy clusters

Jiaxin Han,[1,2,3]★ Carlos S. Frenk,[3] Vincent R. Eke,[3] Liang Gao,[3,4] Simon D. M. White,[5] Alexey Boyarsky,[6,7] Denys Malyshev[7] and Oleg Ruchayskiy[8]

[1]*Key Laboratory for Research in Galaxies and Cosmology, Shanghai Astronomical Observatory, Shanghai 200030, China*
[2]*Graduate School of the Chinese Academy of Sciences, 19A Yuquan Road, Beijing 100049, China*
[3]*Institute for Computational Cosmology, Department of Physics, University of Durham, Science Laboratories, South Road, Durham DH1 3LE*
[4]*Partner Group of the Max Planck Institute for Astrophysics, National Astronomical Observatories, Chinese Academy of Sciences, Beijing 100012, China*
[5]*Max-Planck Institute for Astrophysics, Karl-Schwarzschild Str. 1, D-85748 Garching, Germany*
[6]*Instituut-Lorentz for Theoretical Physics, Universiteit Leiden, Niels Bohrweg 2, Leiden, the Netherlands*
[7]*Bogolyubov Institute of Theoretical Physics, Kyiv, Ukraine*
[8]*CERN Physics Department, Theory Division, CH-1211 Geneva 23, Switzerland*

Accepted 2012 September 7. Received 2012 September 6; in original form 2012 July 29

ABSTRACT

Cold dark matter models predict the existence of a large number of substructures within dark matter haloes. If the cold dark matter consists of weakly interacting massive particles, their annihilation within these substructures could lead to diffuse GeV emission that would dominate the annihilation signal of the host halo. In this work we search for GeV emission from three nearby galaxy clusters: Coma, Virgo and Fornax. We first remove known extragalactic and galactic diffuse gamma-ray backgrounds and point sources from the *Fermi* 2-yr catalogue and find a significant residual diffuse emission in all three clusters. We then investigate whether this emission is due to (i) unresolved point sources, (ii) dark matter annihilation or (iii) cosmic rays (CR). Using 45 months of *Fermi*-Large Area Telescope (*Fermi*-LAT) data we detect several new point sources (not present in the *Fermi* 2-yr point source catalogue) which contaminate the signal previously analysed by Han et al. Including these and accounting for the effects of undetected point sources, we find no significant detection of extended emission from the three clusters studied. Instead, we determine upper limits on emission due to dark matter annihilation and CR. For Fornax and Virgo, the limits on CR emission are consistent with theoretical models, but for Coma the upper limit is a factor of 2 below the theoretical expectation. Allowing for systematic uncertainties associated with the treatment of CR, the upper limits on the cross-section for dark matter annihilation from our clusters are more stringent than those from analyses of dwarf galaxies in the Milky Way. Adopting a boost factor of $\sim 10^3$ from subhaloes on cluster luminosity as suggested by recent theoretical models, we rule out the thermal cross-section for supersymmetric dark matter particles for masses as large as 100 GeV (depending on the annihilation channel).

Key words: astroparticle physics – galaxies: clusters: individual: Coma, Virgo, Fornax – Cosmology: observations – dark matter – gamma-rays: galaxies: clusters.

1 INTRODUCTION

The existence of dark matter (DM) in the Universe has so far only been deduced from its gravitational effect, due to the lack of electromagnetic interactions of the DM with itself or with baryonic matter. There are several elementary particle candidates for DM in various extensions of the standard model of particle physics (Bertone, Hooper & Silk 2004). Weakly interacting massive particles or WIMPs (with a self-interaction cross-section at roughly the weak scale) are one class of the popular DM candidates.

These particles could be related to the electroweak symmetry breaking which is currently being explored by experiments at the Large Hadron Collider (LHC). For example, within the framework of the minimal supersymmetric standard model, the lightest neutralino emerges as a candidate WIMP that is stable over cosmological time-scales and can annihilate into standard model particles.

WIMPs behave as cold DM since their primordial velocity dispersion is negligible. High-resolution *N*-body simulations show that cold DM haloes contain a population of self-bound substructures

★E-mail: jxhan@shao.ac.cn

(subhaloes) whose number decreases with increasing subhalo mass as $N \propto M^{-\alpha}$ with $\alpha \approx 1.9$ (Diemand, Kuhlen & Madau 2007; Springel et al. 2008; Gao et al. 2011)

Much effort has been devoted to the search for WIMPs either directly or indirectly. Direct detection involves identifying the rare events of DM scattering off ordinary matter or searching for new particles near the weak scale at the LHC. Indirect detection involves looking for the annihilation or decay products of DM in cosmic rays (CR) and gamma-rays. In particular, pair annihilation produces gamma-ray photons at a rate proportional to the square of the DM density, which then propagate, almost without absorption, to the observer. In this case, the Galactic Centre should be the brightest gamma-ray source on the sky (Springel et al. 2008, and references therein). Extended emission (distinct from the central point source) was reported from the central 1° around the Galactic Centre by Hooper & Goodenough (2011) and Hooper & Linden (2011b).[1]

This emission has been interpreted as a signal from DM annihilation. There is, however, a strong ambiguity in modelling this region of the Galaxy. Its angular size is comparable with the point spread function (PSF) size of the *Fermi* LAT at these energies and the galactic diffuse background that is known to be complicated and highly non-uniform. In particular, it was demonstrated in Boyarsky, Malyshev & Ruchayskiy (2011) that although an extra diffuse component improves the quality of fit, the radial profile of the 'extended emission' is fully consistent with that of known *Fermi* point sources and therefore the emission could all originate from point sources at the Galactic Centre (see also Abazajian & Kaplinghat 2012). An intriguing aspect of a DM explanation for the gamma-ray emission from the Galactic Centre is that the inferred particle mass of around 10 GeV is also the mass claimed to be required to explain other data, such as the synchrotron emission from the Milky Way's radio filament (Linden, Hooper & Yusef-Zadeh 2011) and the '*Wilkinson Microwave Anisotropy Probe* haze' (Finkbeiner 2004; Hooper, Finkbeiner & Dobler 2007; Hooper & Linden 2011a), as well as signals from the direct detection experiments DAMA/LIBRA (Bernabei et al. 2010), CoGeNT (Aalseth et al. 2011a,b) and CRESST-II (Angloher et al. 2012). These signals, however, could be in tension with other direct detection experiments, such as Cryogenic Dark Matter Search (CDMS; Ahmed et al. 2011) and XENON-100 (Aprile et al. 2011), although optimistic arguments also exist (e.g. Collar 2011a,b). We refer the reader to Hooper (2012) for review.

It has recently been reported that the gamma-ray emission from the region around the Galactic Centre exhibits a line-like excess at energies $\sim$130 GeV (Bringmann et al. 2012; Su & Finkbeiner 2012; Tempel, Hektor & Raidal 2012; Weniger 2012). The interpretation of this signal as arising from DM particles, however, is controversial (see Boyarsky, Malyshev & Ruchayskiy 2012).

Targeting the entire sky rather than the Galactic Centre in searching for annihilation radiation may seem a good strategy since this takes advantage of the large-scale distribution of DM while avoiding some of the uncertainties arising from the astrophysical modelling of galactic gamma-ray sources. However, the fact that we are located near the centre of the Galactic halo and most of the annihilation emission outside the Galactic Centre is produced by DM substructures (Diemand et al. 2007; Springel et al. 2008) results in a gamma-ray map from annihilation that is almost uniform on large scales. This makes detection within the Milky Way halo a difficult task, exacerbated by the additional uncertainty of having to model the extragalactic background, which is more important on large scales (Zaharijas et al. 2010; Baxter & Dodelson 2011).

Dwarf galaxies are the most DM-dominated objects known, are relatively free from astrophysical contamination and appear compact on the sky. They are therefore promising targets to search for DM annihilation radiation. Recent joint analyses of eight to ten dwarf galaxies (Geringer-Sameth & Koushiappas 2011; Ackermann et al. 2011) resulted in no significant detection but have begun to rule out the canonical annihilation cross-section of $3 \times 10^{-26}\,\mathrm{cm^3\,s^{-1}}$ for DM masses below $\sim$30–40 GeV.

Galaxy clusters are the most massive virialized DM structures in the Universe and are also good targets for indirect DM searches. The presence of a large population of DM substructures (or subhaloes) predicted by numerical simulations further enhances the detectability of DM in clusters. Although the total mass within subhaloes amounts to only 10–20 per cent of the total halo mass, the density enhancement within subhaloes can boost the total cluster annihilation luminosity by a factor as high as 1000 when extrapolated down to a subhalo mass limit of $1\,\mathrm{M}_\oplus$, the fiducial cut-off in the primordial power spectrum of density fluctuations for a typical 100 GeV WIMP (Gao et al. 2011; Pinzke, Pfrommer & Bergström 2011). As the distribution of subhaloes is much less concentrated than that of the smooth main halo, the total annihilation emission from clusters is predicted to be extended. Thus, attempts to detect DM annihilation assuming a point source or Navarro–Frenk–White (NFW)-squared profile could miss most of the signal. In fact, just such a search using the 11-month *Fermi*-Large Area Telescope (*Fermi*-LAT) data has yielded no significant detection of emission from six clusters (Ackermann et al. 2010).

Using the 45-month data, we consider possible contributions from CR-induced gamma-ray emission and DM annihilation. For the former (which can be as high as, or higher than, the emission from cluster DM annihilation; Jeltema, Kehayias & Profumo 2009; Pinzke & Pfrommer 2010; Pinzke et al. 2011), we adopt the semi-analytic method developed by Pinzke & Pfrommer (2010). For the later, we adopt the model proposed by Gao et al. (2011) for the cluster DM annihilation profile. We provide constraints on both the CR and DM components for the three galaxy clusters analysed by Han et al. (2012): Coma, which is predicted to have the highest signal-to-noise ratio according to Gao et al. (2011), and Fornax and Virgo which are predicted to have the lowest astrophysical contamination according to Pinzke et al. (2011).

This paper replaces an earlier version by a subset of the authors (Han et al. 2012). After submission of that version, it was pointed out to us that a number of point sources are present in the full 3-yr LAT data which were not detected significantly in the data used for the 'official' *Fermi* point source catalogue available at the time of our analysis, the LAT 2-yr point source catalogue (2FGL; Nolan et al. 2012). We now carry out our own point source detection in the regions of interest and find several new point sources.[2] We account for these new detections in our analysis, as well as for the fact that a significant part of the 'smooth' extragalactic background

[1] See also a preliminary result by the Fermi-LAT collaboration (Vitale et al. 2009).

[2] We notice that several new point sources in Virgo are also identified in a concurrent paper (Macías-Ramírez et al. 2012) and are found to reduce the significance of DM-like emission in the cluster, consistent with what we find here.

Table 1. Data selection criteria.

Minimum energy	100 MeV
Maximum energy	100 GeV
Maximum zenith angle[5]	100°
Event class[6]	3 (P7CLEAN)
DATA-QUAL[7]	1
LAT CONFIG[8]	1
ABS (ROCK ANGLE)[9]	<52°
ROI-based zenith angle cut	yes

is contributed by point sources below the detection threshold; this alters the noise properties of this background. Both changes reduce the significance of the diffuse components apparently detected in the first version of our paper, so that we can now reliably only place upper limits.

Huang, Vertongen & Weniger (2012) have recently reported a failure to detect significant DM annihilation emission from a combined analysis of eight galaxy clusters. Our work differs from theirs in several respects: first, we assume a DM annihilation profile based on high-resolution cosmological simulations (Gao et al. 2011); secondly, we assess the impact of CR in the detection of DM; and finally, we include in our sample the Virgo cluster which turns out to be the best candidate. The constraints we set on the annihilation cross-section are consistent with those of Huang et al. (2012).

The paper is organized as follows. In Section 1 we describe the data and provide an overview of the models of the Virgo, Fornax and Coma galaxy cluster regions used in the analysis (see Table 2). The specification of the non-standard components of the models (DM and CR brightness profiles) is provided in Section 2. The constrains on CR emission and DM annihilation that we obtain are summarized in Section 3 and discussed in Section 4.

The cosmological parameters used in this work are the same as those assumed by Gao et al. (2011): $\Omega_{\rm m} = 0.25$, $\Omega_\Lambda = 0.75$, $h = 0.73$.

1.1 Data preparation

We analyse the first 45 months of data (04/08/2008 to 20/05/2012) from the *Fermi*-LAT,[3] trimmed with the cuts listed in Table 1, to select high-quality photon events. This typically results in $\sim 10^5$ photons within a radius of 10° around each cluster, while the expected number of annihilation photons is of the order of 10^2 according to Fig. 3. The most recent instrument response function (IRF), P7CLEAN_V6, is adopted for the analysis, in accordance with our event class selection.[4] The resulting gamma-ray images for the three clusters are shown in the left-hand panel of Fig. 1 for Virgo and in Fig. C1 for Coma and Fornax.

We list the basic properties of the three clusters in Table 2.

1.2 Maximum likelihood fitting

We use the `pyLikelihood` tool shipped with the FERMI SCIENCE TOOLS software package (version v9r27p1-fssc-20120410) to perform a maximum likelihood (ML) analysis (Mattox et al. 1996). After applying appropriate data cuts, as described in Section 1.1, we bin the data into 0.°1 wide pixels and 30 logarithmic energy bins within a radius of 10° around each cluster. This large radius is chosen to account for the large LAT PSF size at low energies (4° to 10° at 100 MeV[10]). An exposure cube is computed around each cluster covering 25° in radius and the 30 energy bins, using the `gtexpcube2` tool.

In the standard *Fermi* likelihood analysis, the photon counts within each pixel are treated assuming the Poisson statistics for each energy bin to calculate the likelihood. The best-fitting parameters are obtained when the likelihood for the entire data set is maximized. The significance of a given component of interest (e.g. DM or CR) from the ML fitting is quantified by the likelihood ratio statistic,

$$\mathrm{TS} = -2\ln(L_0/L), \tag{1}$$

where L is the ML for the full model and L_0 is the ML for the null hypothesis, i.e. the model *without* the component of interest. According to Wilk's theorem, this test statistic, TS, approximately follows a χ^2 distribution when the null hypothesis is true, with one degree of freedom for our case where the normalization is the only extra parameter in the alternative model. The probability that a given value of TS arises purely from fluctuations of the null hypothesis is

$$P = \int_{\rm TS}^{\infty} \frac{1}{2}\chi_1^2(\xi)\,\mathrm{d}\xi = \int_{\sqrt{\rm TS}}^{\infty} \frac{\mathrm{e}^{-x^2/2}}{\sqrt{2\pi}}\,\mathrm{d}x. \tag{2}$$

The factor $\frac{1}{2}$ comes from the constraint that the normalization parameter be non-negative. The significance of a detection can thus be quoted as $\sqrt{\mathrm{TS}}\sigma$ (one-sided Gaussian confidence). Upper limits on the extra normalization parameter N are obtained by searching for a null hypothesis L_0', where N in the full model is constrained to be equal to the upper limit, $N_{\rm UL}$, so that $\ln(L_0'/L) = -1.35$, corresponding to the 95 per cent confidence interval.

1.3 Model

For the analysis we constructed a model to fit the data including all known foreground and background emission, as well as DM and CR components, as appropriate. We include all the point sources from 2FGL within a radius of 15° from the cluster centre in the model, plus the most recent galactic (GAL) and extragalactic (EG) diffuse emission given by the template files `gal_2yearp7v6_v0.fits` and `iso_p7v6clean.txt`. Additionally, we have searched the 45-month data for new point sources; we detect several of them within the cluster region (see Appendix A for more detail) and these are also included in our model. The normalizations of the GAL and EG diffuse components are allowed to vary during the fitting. Within the cluster virial radius there are two 2FGL point sources and one newly detected point source in Fornax, six 2FGL, including the central AGN (M87; Abdo et al. 2009), plus four newly

[3] http://fermi.gsfc.nasa.gov/cgi-bin/ssc/LAT/LATDataQuery.cgi

[4] We also tried using P7SOURCE_V6 IRF and Event Class 2 data. The results are consistent with those presented in this paper.

[5] ZENITH ANGLE (degrees): angle between the reconstructed event direction and the zenith line (originates at the centre of the Earth and passes through the centre of mass of the spacecraft, pointing outwards). The Earth's limb lies at a zenith angle of 113°.

[6] EVENT CLASS: flag indicating the probability of the event being a photon and the quality of the event reconstruction.

[7] DATA-QUAL: flag indicating the quality of the LAT data, where 1 = OK, 2 = waiting review, 3 = good with bad parts, 0 = bad.

[8] LAT-CONFIG: flag for the configuration of the lat (1 = nominal science configuration, 0 = not recommended for analysis).

[9] ROCK ANGLE: angle of the spacecraft z-axis from the zenith (positive values indicate a rock towards the north).

[10] The LAT PSF size scales roughly as $E^{-0.8}$, so at 1 GeV it is $\sim 1°$.

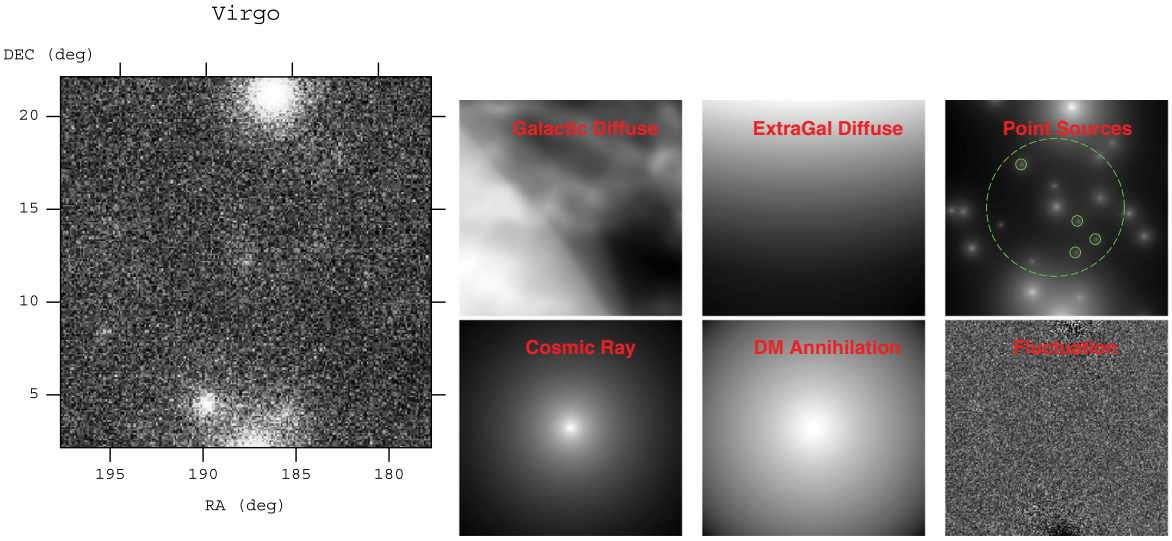

Figure 1. Decomposition of the *Fermi*-LAT image in the region of the Virgo cluster into model components. The observed photon count image from 100 MeV to 100 GeV is shown on the left. The right-hand panels show the integrated image over the same energy range for the various model components: galactic diffuse emission, extragalactic diffuse emission, detected point sources, CR photons and DM annihilation emission, as labelled. The green dashed circle in the 'Point sources' panel marks the virial radius of the cluster. The small circles mark the newly detected point sources which are not present in the 2FGL. The 'Fluctuation' panel shows the residual image for our best-fitting DM model. The images have been enhanced individually in colour space for contrast. Note the apparent structure in the extragalactic component which is due to different exposure times at different positions.

Table 2. Basic properties of target clusters.

	Coma	Fornax	Virgo (M87)
RA (°)	194.9468	54.6686	187.6958
Dec. (°)	27.9388	−35.3103	12.3369
D_A (Mpc)[a]	95.8	17.5	16.8
M_{200} ($M_\odot$)[b]	1.3e15	2.4e14	7.5e14
r_{200} (°)[b]	1.3	4.1	6.2
$\mathcal{J}_{NFW}$[c]	5.9e−5	4.1e−4	1.2e−3
Enhancement due to subhaloes within r_{200} [d]	1.3e3	6.5e2	1.0e3

[a]Angular diameter distance, from the NASA extragalactic data base for Coma and Fornax, and from Tully & Shaya (1984) for Virgo.
[b]Cluster halo mass defined as the mass within the radius, r_{200}, within which the average density equals 200 times the critical density of the Universe. Values for Coma and Fornax are taken from Pinzke et al. (2011), while the value for Virgo is taken from Tully & Shaya (1984).
[c]Integrated coefficient, $\mathcal{J}_{int} = \int_{\Delta\Omega} J\,d\Omega$, over the solid angle spanned by the cluster virial radius, assuming a smooth NFW density profile.
[d]Enhancement to the total annihilation luminosity within the virial radius due to substructures, extrapolated to a subhalo mass limit of $10^{-6}\,M_\odot$. Note that this factor scales with the minimum subhalo mass as $M_{cut}^{-0.226}$ (Springel et al. 2008).

detected ones in Virgo. We allow the normalization and power-law spectral index of these 13 point sources to vary freely. In addition, the parameters of all sources with variability index greater than 50 located within 10° of the cluster centres are allowed to vary. Parameters for the other point sources are fixed as in the 2FGL catalogue. From now on we refer to the model with GAL, EG and the known point sources as the 'base model'.

A DM annihilation surface brightness template (given by the dimensionless factor J; see equation 4 in Section 2.1) is generated for each cluster out to a 15° radius by summing up both the contribution from a smooth NFW profile and the contribution from subhaloes. This J map is used to fit for extended cluster annihilation emission. For the point source model, the integrated factor $\mathcal{J}_{NFW}$ (see equation 5) is used to derive an annihilation cross-section from the fitted total flux. Similarly, a CR photon template is generated for each cluster out to three times the cluster virial radius, where the surface brightness has dropped to below 10^{-5} of the central value and beyond which the model is not reliable. Images for various model components are shown in Fig. 1 taking Virgo as an example. We discuss these templates in more detail in Section 2.

In the traditional *Fermi* analysis, the EG template is treated as a smooth component where all emission below the nominal point source detection limit is assumed to come from a smoothly distributed diffuse component. In this work, we also consider a more realistic one where a fraction is assumed to be contributed by fainter point sources with a number–flux relation which extrapolates smoothly from that measured for brighter sources. In this case the photon counts within a given pixel are no longer Poisson distributed since the photons arrive in packets. In principle, one

can use the full distribution of photon counts from a population of randomly placed point sources to calculate the likelihoods L and L_0, but equations (1) and (2), and the corresponding discussion, are not affected. However, since the full distribution of photon counts in this case (Han et al., in preparation) is complicated and difficult to implement in the likelihood analysis, instead of recalculating L and L_0, in this work we use Monte Carlo simulations to re-evaluate the distribution of TS for the more realistic background model and provide corrections to the results of the standard analysis where needed.

2 MODELING GAMMA-RAY EMISSION IN CLUSTERS

We model the observed gamma-ray emission in clusters with several components as shown in Fig. 1: the galactic foreground (GAL), the extragalactic background (EG), emission from known point sources, DM annihilation and CR-induced emission. The GAL and EG diffuse emission are given by the most recent templates, `gal_2yearp7v6_v0.fits` and `iso_p7v6clean.txt`, which can be obtained from the *Fermi*-LAT data server, while the point sources include those from the LAT 2-yr point source catalogue, 2FGL (Nolan et al. 2012), as well as several, newly detected by us, in the 45-month data. In addition, an improved EG model which includes a population of undetected sources is also analysed. We now describe in detail our models for DM annihilation and CR emission.

2.1 DM annihilation emission

The gamma-ray intensity along the line of sight due to DM annihilation is given by

$$I = \frac{1}{8\pi}\sum_f \frac{\mathrm{d}N_f}{\mathrm{d}E}\langle\sigma_f v\rangle \int_{\mathrm{l.o.s.}} \left(\frac{\rho_\chi}{M_\chi}\right)^2 (l)\ \mathrm{d}l, \tag{3}$$

where M_χ is the DM particle mass; ρ_χ the density of DM; $\frac{\mathrm{d}N_f}{\mathrm{d}E}$ the particle model-dependent term giving the differential number of photons produced from each annihilation event as a function of energy, E, in a particular annihilation channel, f; and $\langle\sigma_f v\rangle$ is the velocity-averaged cross-section (or annihilation rate) for that channel, which is predicted to be constant in the low-velocity limit appropriate to present-day cold DM particles (see e.g. Jungman, Kamionkowski & Griest 1996). The line-of-sight integration of the density squared is often expressed in terms of a dimensionless factor,

$$J = \frac{1}{8.5\,\mathrm{kpc}}\left(\frac{1}{0.3\,\mathrm{GeV\,cm^{-3}}}\right)^2 \int_{\mathrm{l.o.s.}} \rho_\chi^2(l)\ \mathrm{d}l. \tag{4}$$

If the source size is much smaller than the instrumental beam size, a point source approximation is applicable. In this case, the integration of J over a large enough solid angle, $\Delta\Omega$, is used to determine the total flux for the point source, $\mathcal{J}_{\mathrm{int}} = \int_{\Delta\Omega} J\,\mathrm{d}\Omega$.

The cluster annihilation emission is modelled with the extended profile suggested by Gao et al. (2011). However, for part of the analysis and for comparison purposes, we will also use the point source approximation which, although inappropriate, has been employed in all previous analyses of *Fermi*-LAT data from clusters. We shall refer to models that assume these two profiles, respectively, as EXT and PT. If the cluster follows a smooth NFW profile, then its integrated J factor which determines the total annihilation flux can be found as

$$\mathcal{J}_{\mathrm{NFW}} = \frac{4\pi}{3}\rho_s^2 r_s^3 \frac{1}{D_{\mathrm{A}}^2} \times \frac{1}{8.5\,\mathrm{kpc}}\left(\frac{1}{0.3\,\mathrm{GeV\,cm^{-3}}}\right)^2. \tag{5}$$

Here D_{A} is the angular diameter distance to the cluster and ρ_s and r_s are the characteristic density and radius of the NFW profile. They are related to halo concentration, c, and virial radius through the relations, $\rho_s = \frac{200}{3}\frac{c^3\rho_{\mathrm{c}}}{\ln(1+c)-c/(1+c)}$ and $r_s = r_{200}/c$, with ρ_{c} the critical density of the Universe, r_{200} the cluster virial radius within which the average density is $200\rho_{\mathrm{c}}$, and the concentration parameter, c, is given by the following mass–concentration relation (Duffy et al. 2008):

$$c = 5.74\left(\frac{M_{200}}{2\times10^{12}\,h^{-1}\,\mathrm{M_\odot}}\right)^{-0.097}. \tag{6}$$

Here, M_{200} is the mass enclosed within r_{200}. Extrapolating to a cutoff mass of $10^{-6}\,\mathrm{M_\odot}$, the existence of subhaloes will increase this flux by a factor (Gao et al. 2011)

$$b(M_{200}) = \mathcal{J}_{\mathrm{sub}}/\mathcal{J}_{\mathrm{NFW}} = 1.6\times10^{-3}(M_{200}/\mathrm{M_\odot})^{0.39}. \tag{7}$$

Using the results of the simulations by these authors, the surface brightness profile of subhalo emission can be fitted within r_{200} by the formula

$$J_{\mathrm{sub}}(r) = \frac{16b(M_{200})\mathcal{J}_{\mathrm{NFW}}}{\pi\ln(17)}\frac{D_{\mathrm{A}}^2}{r_{200}^2+16r^2} \quad (r\le r_{200}). \tag{8}$$

Below we fit the subhalo emission surface brightness beyond the virial radius and extrapolate to several times the virial radius using an exponential decay,

$$J_{\mathrm{sub}}(r) = J_{\mathrm{sub}}(r_{200})\mathrm{e}^{-2.377(r/r_{200}-1)} \quad (r\ge r_{200}). \tag{9}$$

The total annihilation profile is the sum of the contributions from a smooth NFW profile and the subhalo emission. This is completely dominated by subhalo emission except in the very centre of the cluster. We show the total annihilation profile and its decomposition into main halo and subhalo contributions in the left-hand panel of Fig. 3, taking Virgo as an example. This profile is further inflated after convolution with the LAT PSF.

We consider three representative annihilation channels, namely into $b-\bar{b}$, $\mu^+-\mu^-$ and $\tau^+-\tau^-$ final states. The annihilation spectrum is calculated using the DARKSUSY package (Gondolo & Silk 1999),[11] which tabulates simulation results from PYTHIA.[12] We also include the contribution from inverse Compton (IC) scattered photons by energetic electron–positron pairs produced during the annihilation process, following the procedure described in Pinzke et al. (2011). In general, three external energy sources are involved in the dissipation and scattering of the injected electrons from annihilation: the cosmic microwave background (CMB), infrared to ultraviolet light from stars and dust, and the interstellar magnetic field. However, as shown by Pinzke et al. (2011), the latter two components are expected to be important only in the inner region of clusters ($<0.03r_{200}$), corresponding to less than 0.2 for our three clusters. Including them would introduce a position-dependent component to the annihilation spectrum, so for simplicity we only consider the contribution of CMB photons in the IC calculation. For the $b\bar{b}$ channel, IC photons only contribute significantly to the low-energy spectrum for relatively high neutralino mass, while for the leptonic channels, which have plenty of energetic electrons, the IC emission can completely dominate the annihilation emission over the full energy range of interest for the highest neutralino masses considered.

We note that the electroweak corrections recently proposed by Ciafaloni et al. (2011) (see also Cirelli et al. 2011) can bring visible

[11] http://www.darksusy.org
[12] http://home.thep.lu.se/ torbjorn/Pythia.html

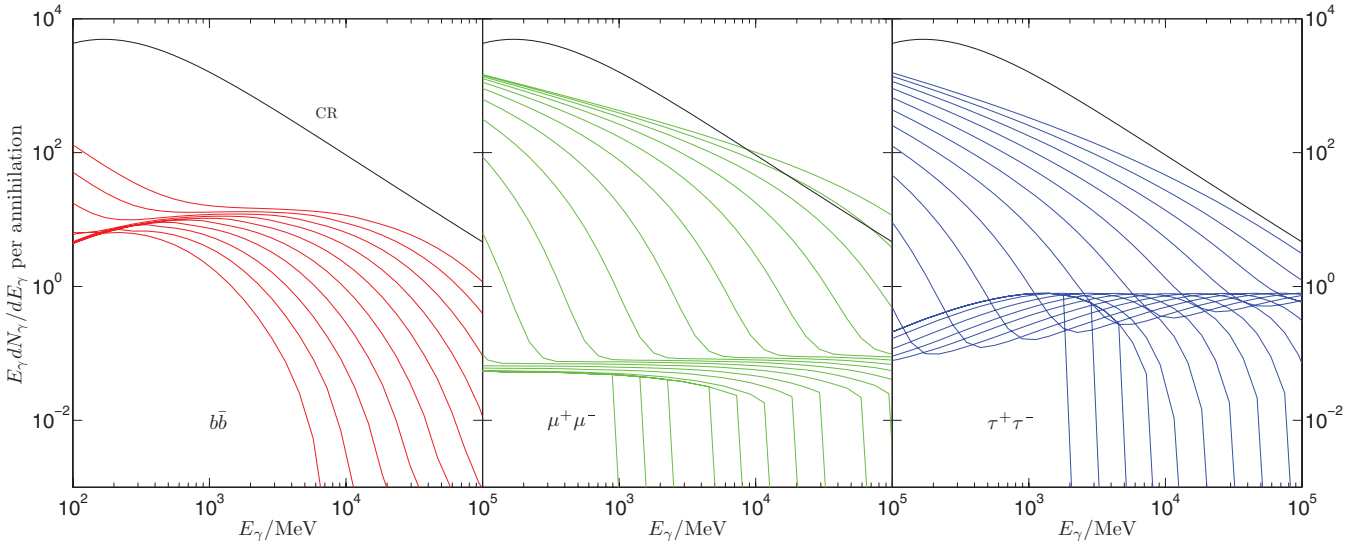

Figure 2. Photon yields for $b\bar{b}$ (left), $\mu^+\mu^-$ (middle) and $\tau^+\tau^-$ (right) channels. Plotted are the total photon yields including continuum secondary photons, final-state radiation from charged final-state particles, as well as IC scattering of CMB photons by electron/positron pairs, for the mass range 10–1000 GeV for the $b\bar{b}$ channel, 1 GeV–10 TeV for the $\mu^+\mu^-$ channel and 2 GeV–10 TeV for the $\tau^+\tau^-$ channel. The masses are sampled uniformly in a log scale. Note that each spectrum cuts off at an energy corresponding to the particle mass. For comparison, the black line in each panel shows the photon spectrum from CR-induced photons with arbitrary normalization.

differences to the leptonic channel spectra at high WIMP masses before IC scattering. However, since IC photons dominate at the high-mass end and the electroweak correction only significantly changes the positron yields at low energy, thus having little effect on the IC spectrum, the electroweak correction to the total spectrum is still negligible. The total photon yields are shown in Fig. 2. The almost flat spectrum with a cutoff around the energy corresponding to the WIMP mass comes from prompt annihilation emission including continuum secondary photons and final-state radiation from charged final-state particles. The low energy rise originates from IC scattered CMB photons.

2.2 CR-induced gamma-ray emission within clusters

The CR-induced gamma-ray emission is calculated following a semi-analytic prescription, derived from high-resolution numerical simulations of galaxy clusters, that models CR physics self-consistently (Pinzke & Pfrommer 2010). The gamma-ray photon production rate (or the source function) from pion decay is found to be separable into a spatial and a spectral part:

$$q_{\rm CR}(r, E) \equiv \frac{{\rm d}N_\gamma}{{\rm d}t\,{\rm d}V\,{\rm d}E} = A(r)s(E), \tag{10}$$

where the spatial part, $A(r)$, is proportional to the square of the gas density profile multiplied by a slowly varying radial function parametrized by cluster mass. The spectral part, $s(E)$, is almost independent of cluster mass and has a power-law form, ${\rm d}N_\gamma/{\rm d}\ln(E_\gamma) \propto E_\gamma^{-1.3}$, for the energy range 1−100 GeV but flattens at low energies, as shown in Fig. 2. We summarize the detailed form of $A(r)$ and $s(E)$ plus the gas density profile for the three clusters derived from X-ray observations in Appendix D.

The differential gamma-ray flux from this source function, $I_{\rm CR}(r, E)$, is simply the integral of $q_{\rm CR}(r, E)$ along the line of sight. This prescription is derived from the average emission profile for a sample of simulated clusters for a realistic choice of parameter values (e.g. for the maximum shock acceleration efficiency, $\zeta_{p,\rm max}$). In addition to the uncertainties in the model parameters, there is also uncertainty in the observationally derived halo mass and gas density profile. In this work, we simply assume that the shape of $q_{\rm CR}(r, E)$ is given by the model described above and account for the uncertainty in the model parameters, as well as sample variance with an additional normalization parameter, $\alpha_{\rm CR}$, so that

$$I_{\rm CR}(r, E) = \alpha_{\rm CR} \int_{\rm l.o.s} \frac{q_{\rm CR}(r, E)}{4\pi} {\rm d}l. \tag{11}$$

We take $\alpha_{\rm CR} = 1$ as our fiducial CR model and also consider the case when $\alpha_{\rm CR}$ is fitted from the actual gamma-ray data as an optimal model. In the right-hand panel of Fig. 3 we compare the CR profile for the fiducial model to the expected DM annihilation profile within our three clusters, assuming a fiducial DM particle model with particle mass $M \approx 100$ GeV, annihilating through the $b\bar{b}$ channel with cross-section $\langle\sigma v\rangle = 3 \times 10^{-26}$ cm^3 s^{-1}. In general, the CR emission is more centrally concentrated than the annihilation profile since the CR trace the gas profile. It can be readily seen that Fornax has a particularly low CR level, while Coma is CR dominated. Coma has steeper profiles due to its larger distance and hence smaller angular size.

3 RESULTS

3.1 Constraints on CR emission

With all the model components defined above, we first proceed with ML fitting for a model with no DM annihilation but with cosmic rays, the 'CR-only' model hereafter. Note that the GAL and EG backgrounds, as well as the nearby point sources, are always included in the analysis, as described in Section 1.2. The results for the CR-only model fits are listed in Table 3. The fitted CR levels all agree within a factor of 3 with the theoretical predictions. While Fornax is most consistent with no CR emission due to its intrinsically low CR level, the derived upper limit for Coma already rules out the fiducial value at 95 per cent confidence.

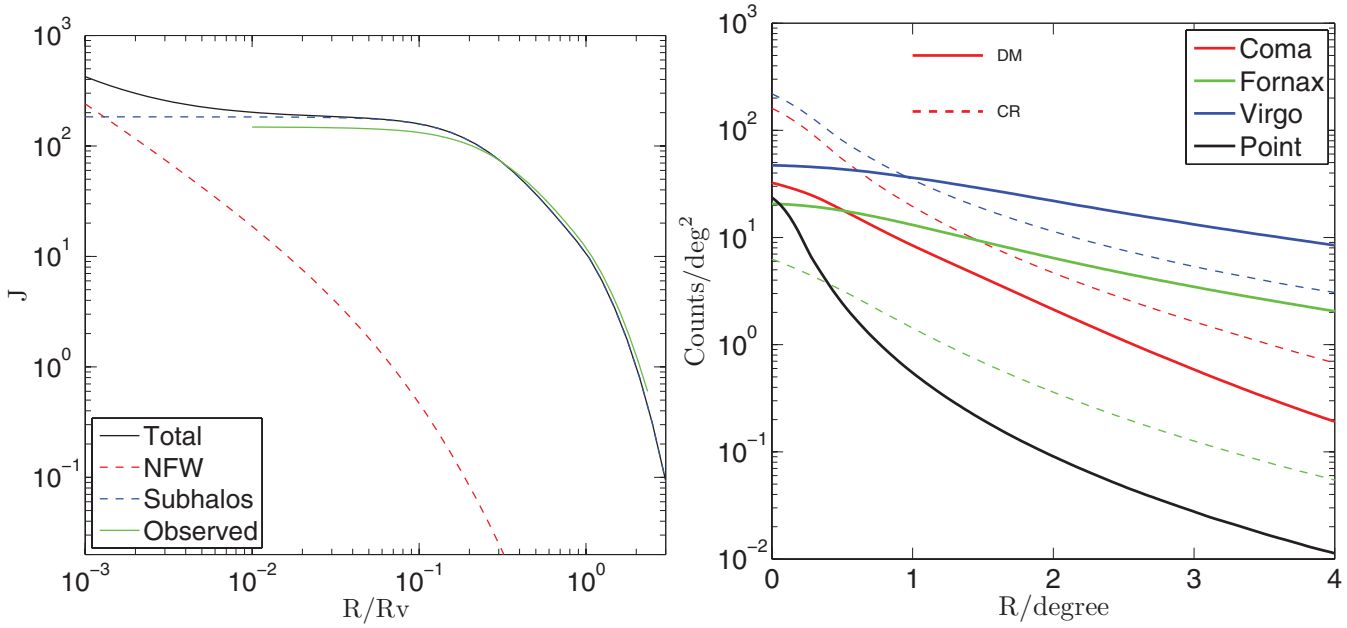

Figure 3. Cluster photon profiles. Left: theoretical and PSF-convolved J profile for Virgo. The total annihilation profile is shown as a black solid line and is decomposed into the smooth main halo part (red dashed line) and the subhalo part (blue dashed line). The green solid line shows the annihilation profile after PSF convolution, plotted down to an inner radius comparable to the pixel size of 0.1°. Right: PSF-convolved photon profiles from annihilation (solid) and CR (dashed) for three clusters (indicated by different colours). The solid lines show the expected photon count profile for the extended DM annihilation model. The dashed lines show the expected CR-induced photon counts for the fiducial CR model. For comparison, we also plot the PSF-convolved profile for a central point source (black solid line) with arbitrary normalization. In both panels, a DM model with particle mass, $M \approx 100$ GeV, and annihilation cross-section, $\langle \sigma v \rangle = 3 \times 10^{-26}\,\mathrm{cm^3\,s^{-1}}$, through the $b\bar{b}$ channel is assumed. The PSF convolutions are done with the `gtmodel` tool in the FERMI SCIENCE TOOLS software package.

Table 3. Fits to the CR-only model.

	$\alpha_{\mathrm{CR,fit}}{}^a$	$\alpha_{\mathrm{CR,UL}}{}^b$	$F_{\mathrm{CR,UL}}{}^c$ (ph cm^{-2} s^{-1})	TS	$\mathrm{TS_{corrected}}{}^d$	$\alpha_{\mathrm{CR,UL,corrected}}{}^e$
Coma	0.3 ± 0.1	0.5	2.4e−09	5.2	2.6	0.6
Fornax	0.9 ± 2	4.8	1.8e−09	0.2	0.1	6.4
Virgo	0.6 ± 0.3	1.2	2.1e−08	8.4	2.8	1.6

[a]Best-fitting normalization ($\alpha_{\mathrm{CR,fit}} = 1$ is the theoretical prediction).
[b]95 per cent upper limit (UL) on the normalization.
[c]95 per cent upper limit on the CR-induced gamma-ray flux from 100 MeV to 100 GeV.
[d]TS after allowing for undetected point sources; see Section 3.3 for details.
[e]Upper limit on the normalization factor after allowing for undetected point sources; see Section 3.3 for details.

3.2 Constraints on DM annihilation

Given the low significance of the CR detection in the CR-only model, it is not safe simply to adopt the best-fitting α_{CR} values for further extraction of the DM signal. Instead, we consider the following four families of CR models in the presence of a DM component.

(1) *Fiducial-CR model*. The CR level is fixed to the theoretical expectation $\alpha_{\mathrm{CR}} = 1$. Since this value exceeds our derived upper limit for Coma, we exclude Coma from further discussion of this family.

(2) *Optimal-CR model*. The CR level is taken as the best-fitting value listed in Table 3.

(3) *Free-CR model*. The normalization of the CR level is left as a free parameter in the fit.

(4) *No-CR model*. No CR emission is considered, only DM.

For each family, both point source (PT) and extended (EXT) profiles are considered for the DM component (the former merely for comparison with earlier work). Note that when calculating the TS for DM, the null hypothesis refers to the full model excluding only the DM component or, equivalently, to the base model plus a CR component modelled according to one of our four families of CR models. We show results for the $b\bar{b}$, $\mu^+\mu^-$ and $\tau^+\tau^-$ DM annihilation channels.

For none of the combinations of DM and CR models considered here, do we obtain a detection of DM at high significance in any of the three clusters. The highest significance is obtained for Virgo for the $b\bar{b}$ channel in a DM model that has a particle mass of 30 GeV and the EXT profile, in the absence of CR. In this case, we find TS = 11.6, corresponding to 3.4σ. This reduces to 2.6σ in the free-CR model and to less than 1σ in the fiducial-CR model.

The value of TS = 11.6 for the no-CR model for Virgo can be compared with the value of TS = 24 reported in an earlier version of this paper (arXiv:1201.1003v.1) from a similar analysis of the 3-yr Virgo data (see Fig. 4). The decrease in significance is entirely due to the subtraction of the new point sources which we have detected in the Virgo region and which were not catalogued in the 2FGL. These previously undetected sources happen to lie within the virial

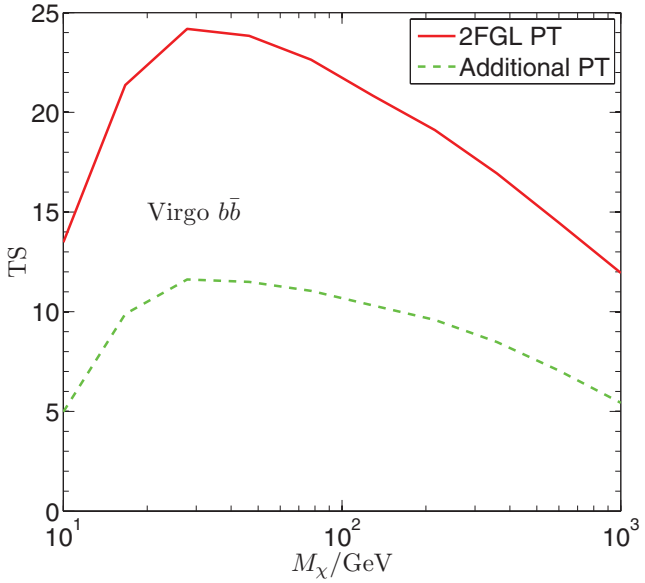

Figure 4. The significance of a DM component in Virgo, with $b\bar{b}$ final states, in the absence of CR. The solid line shows the TS when only 2FGL sources are included in the model, while the dashed line shows the case when the four new point sources that we have detected are also included.

radius of Virgo and can mimic the extended emission expected from DM annihilation. In fact, fits assuming an EXT profile and a power law, rather than a DM annihilation spectrum, result in a similarly high-significance detection, TS = 21, and a best-fitting spectral index $\Gamma = -1.9$. This is the typical spectral index of *Fermi* point sources (including the newly detected ones). The preference for a 30-GeV DM particle mass in the DM fits reflects a preference for a $\Gamma = -1.9$ spectrum around 1 GeV, the energy scale from which most of the significance arises.

In fact, the significance of the Virgo detection is further reduced when we take account of a possible undetected point source population in the analysis, as we shall do in Appendix B. Thus, in what follows we use our analysis exclusively to set upper limits on the flux and annihilation cross-section.

3.2.1 *The $b\bar{b}$ channel*

In Fig. 5 we show the 95 per cent confidence upper limits on the DM annihilation flux and compare them to the CR levels. For each cluster, the coloured stripes are defined by the minimum and maximum upper limits corresponding to the four families of CR models. The optimal CR levels in the three clusters are all comparable to the fitted DM flux, and the DM flux upper limits for the four different CR models vary only within a factor of 2, with the no-CR and fiducial-CR[13] cases predicting the highest and lowest upper limits. The left- and right-hand panels show the results for the EXT and PT models, respectively; the PT models always have lower flux upper limits than the extended models.

The flux upper limits are translated into cross-section upper limits in Fig. 6, using equation (3). These are also shown as coloured regions reflecting the variation in the different treatments of CR. Although the predicted flux upper limits decrease slowly with DM particle mass and remain within the same order of magnitude for the mass range considered, the resulting cross-section upper limits increase by a factor of 100 from low to high particle mass. This is because low-mass particles correspond to higher DM number densities (the ρ_χ^2/M_χ^2 factor in equation 3) for a given mass density, so to obtain the same flux level, the required cross-section must be smaller for low-mass particles. With an enhancement of the order of 10^3 due to subhaloes, a much lower cross-section is needed (by a factor of at least 100) for extended annihilation models to achieve a slightly higher flux upper limit than point source models.

Our cross-section limits drop below the fiducial thermal cross-section of $3 \times 10^{-26}\mathrm{cm}^3\,\mathrm{s}^{-1}$ for $M_\chi \lesssim 100$ GeV. Of the three clusters, Virgo has the highest flux upper limits but it still places the tightest constraints on the annihilation cross-section. Our limits are much lower than those in the 11-month *Fermi*-LAT analysis by Ackermann et al. (2010), where the tightest constraint came from Fornax for a much lower assumed subhalo contribution of ∼10. Our limits are also tighter than those from a joint analysis of the dwarf satellites of the Milky Way by Geringer-Sameth & Koushiappas (2011).[14] Note that the difference between our results and those of Ackermann et al. (2010) comes mostly from different assumptions about the effect of subhaloes, and only secondarily from the larger amount of data we have analysed. Also, note that in the analysis of Geringer-Sameth & Koushiappas (2011), no boost from subhaloes within the halo of dwarf galaxies was assumed.

3.2.2 *The $\mu^+\mu^-$ channel*

As have been seen in Section 3.2.1, the EXT model places tighter constraints on the cross-section than the PT model and is the fiducial model expected from recent simulations. Therefore, from now on we will only show results for the EXT model. The flux and cross-section upper limits for DM annihilating through the $\mu^+\mu^-$ channel are plotted in Figs 7 and 8. The predicted flux upper limits for Coma and Virgo are still comparable to the CR level, with Fornax having much lower CR emission. The inferred cross-section falls below the canonical value for DM particle masses less than 10 GeV. Note the discontinuity in the upper limits around 100 GeV which reflects the transition from the prompt-annihilation-dominated regime to the IC-emission-dominated regime in the photon spectrum.

3.2.3 *The $\tau^+\tau^-$ channel*

In Fig. 9 we show the cross-section upper limits for the $\tau^+\tau^-$ channel. This is the primary component of the leptonic model used by Hooper & Linden (2011b) to fit the excess gamma-ray emission in the Galactic Centre region.

3.3 Allowing for an undetected point source population

Although we have detected five new point sources in the 45-month data in the region of our three clusters, it is still necessary to account for the population of still undetected point sources. When no unknown point sources are present, the probability of measuring a certain value of TS when the null hypothesis is true is given by the probability that Poisson fluctuations in the photon counts for the null model exceed some value. When a population of undetected point sources is present, the Poisson fluctuations become correlated and it is easier for the same amplitude of fluctuations to result in

[13] In Coma, where the fiducial-CR model is ruled out, the optimal-CR model yields the lowest upper limit.

[14] If systematic uncertainties in the halo mass parameters assumed by Geringer-Sameth & Koushiappas (2011) are considered, the lower bounds of their derived limits become comparable to our limits.

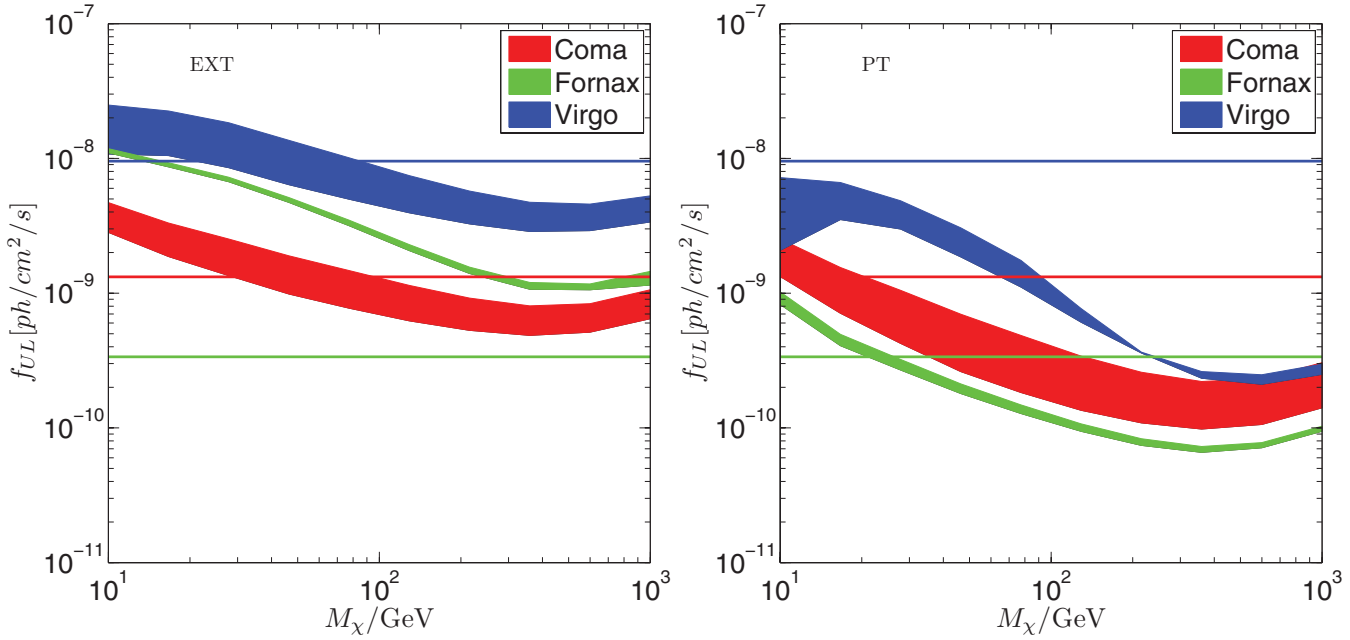

Figure 5. DM annihilation flux upper limits for the $b\bar{b}$ channel. The stripes are defined by the minimum and maximum upper limits given by the four CR model families, with different colours corresponding to different clusters, as indicated in the legend. Left- and right-hand panels show the results for the EXT and PT profiles, respectively. For each cluster, a solid line of the corresponding colour shows the optimal CR flux.

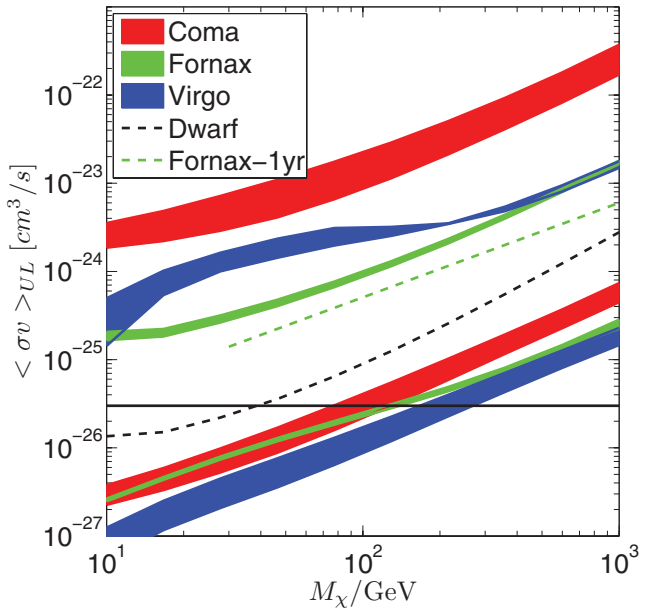

Figure 6. Upper limits for the DM annihilation cross-section in the $b\bar{b}$ channel. The different colours represent the three clusters, with the stripes spanning the range between the minimum and maximum upper limits given by the four different ways of treating the CR component. The three highest stripes show the PT model constraints and the three lowest the EXT model constraints. We also plot with dashed lines constraints (The 'Fermi-1yr' constraint is only reproduced schematically, by reading out several data points from the original plot in the reference.) from a joint analysis of the Milky Way dwarf galaxies (Geringer-Sameth & Koushiappas 2011, black dashed line) and previous constraints from the 11-month *Fermi*-LAT data for Fornax (Ackermann et al. 2010, green dashed line) assuming these authors' optimistic value for the total enhancement due to subhaloes, which gives the tightest constraint. The black solid line indicates the canonical thermal cross-section of 3×10^{-26} cm^3 s^{-1}.

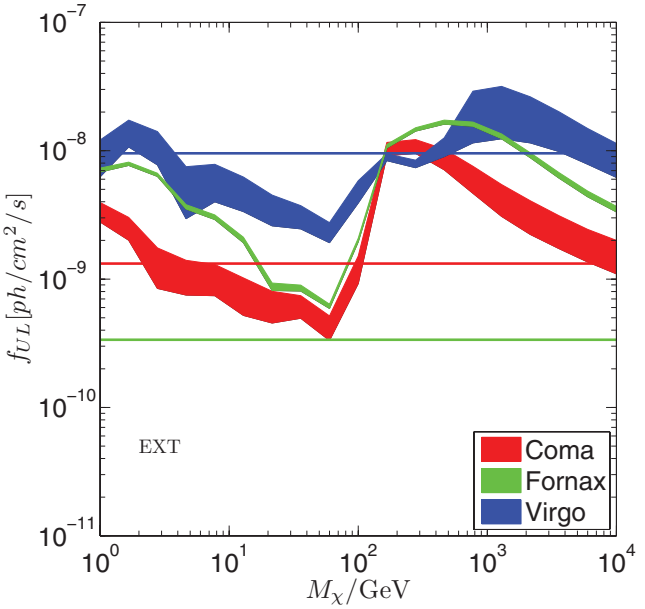

Figure 7. DM annihilation flux upper limits in the $\mu^+\mu^-$ channel for the EXT model. The line styles are as in Fig. 5.

a given value of TS. In this case, the distribution of TS no longer follows the χ^2 distribution, as predicted by Wilk's theorem, because the data no longer follow a pure Poisson distribution from which the likelihood function is constructed.

Allowing for the presence of undetected point sources in the data will lead to weaker upper limits. We obtain these by performing Monte Carlo simulations to re-calibrate the significance corresponding to a given value of TS. In the simulations we include the GAL and 2FGL sources, but we split the EG component into two parts: a population of undetected point sources and a residual smooth EG component, such that the sum of the two is consistent

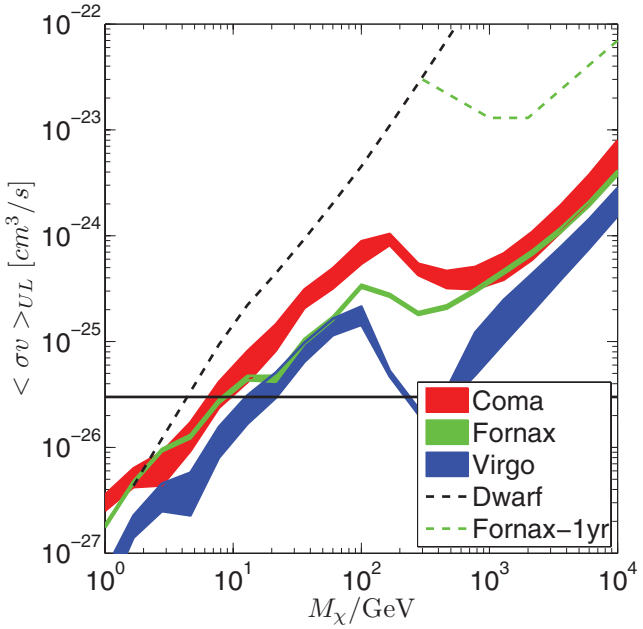

Figure 8. Upper limits for the DM annihilation cross-section in the $\mu^+\mu^-$ channel. The line styles are as in Fig. 6, but only the EXT results are shown. The green dashed line shows the 11-month *Fermi* result (Ackermann et al. 2010) for Fornax, while the black dashed line shows the dwarf galaxy constraint (Geringer-Sameth & Koushiappas 2011), both for the $\mu^+\mu^-$ channel.

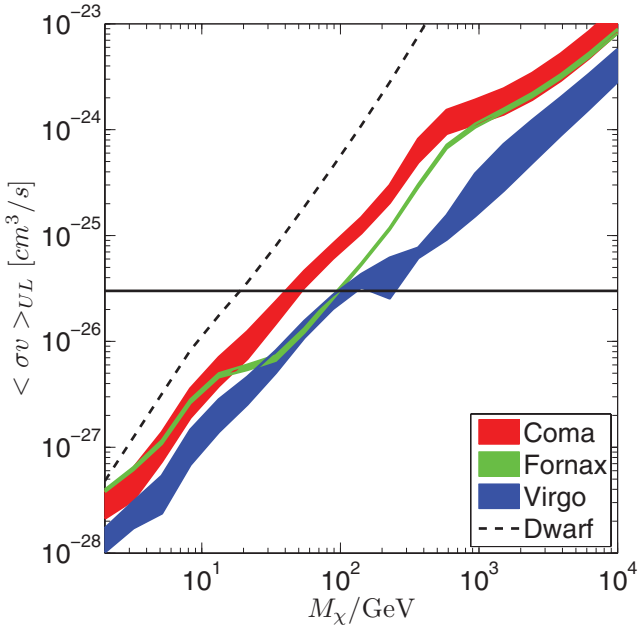

Figure 9. Upper limits for the DM annihilation cross-section in the $\tau^+\tau^-$ channel. The line styles are as in Fig. 6, but only the EXT results are shown. The black dashed line shows the dwarf galaxy constraint (Geringer-Sameth & Koushiappas 2011).

with the standard EG component. We consider a benchmark model for the undetected point source population which is close to the model derived by Abdo et al. (2010) and which contributes 14 per cent of the EG background. Details of the simulations may be found in Appendix B. A standard likelihood analysis is then performed on the simulated data in order to derive appropriate values of TS for an assumed DM or CR component.

With the introduction of the undetected point source population, the distribution function for TS is found to be roughly described by $\chi^2(\mathrm{TS}/b)/2$. That is, the significance of a given value of TS is approximately reduced by a factor of b compared to the significance of the same value of TS in the absence of the undetected point source population. For a DM component, we find $b \sim 2$ for Coma and $b \sim 3$ for Virgo and Fornax. The b factor is not sensitive to the adopted DM spectrum. For the CR models, we find $b \sim 2$ for Coma and Fornax, and $b \sim 3$ for Virgo.

In order to obtain new limits from the corrected TS, let us first consider the likelihood function that has been maximized over all the nuisance parameters. Expanding around the ML value of the parameter N to leading order, we have

$$\ln L(N_0) = \ln L(N) - \frac{1}{2}H(N_0 - N)^2, \tag{12}$$

where $H = -\frac{\mathrm{d}^2 \ln L}{\mathrm{d}N^2} = \frac{1}{\sigma_N^2}$ is the Hessian matrix. The 95 per cent upper limit is calculated from $\ln L(\mathrm{UL}) - \ln L(N) = -1.35$, so that

$$\mathrm{UL} = N + 1.64\sigma_N. \tag{13}$$

Note that $\frac{N}{\sigma_N} = \sqrt{\mathrm{TS}}$. Similar equations hold for the improved background model, with UL, σ_N and TS replaced by UL′, σ_N' and TS′, respectively, assuming that there is no bias in the best-fitting parameters. The 95 per cent upper limit is then corrected for the undetected point source fluctuations according to

$$\mathrm{UL}' = \frac{\sqrt{\mathrm{TS}} + 1.64\sqrt{\mathrm{TS}'/\mathrm{TS}}}{\sqrt{\mathrm{TS}} + 1.64}\mathrm{UL}, \tag{14}$$

where UL and TS are the upper limit and likelihood ratio from the standard analysis, while UL′ and TS′ are the corrected upper limit and likelihood ratio. For $b = 3$, the increase in the upper limit is at most 70 per cent.

In Fig. 10, we show the corrected DM annihilation cross-section upper limits adopting $b = 2$ for Coma and $b = 3$ for Virgo and Fornax. The corrected TS and upper limits for CR models are listed in the last two columns of Table 3.

4 DISCUSSION AND CONCLUSIONS

We have performed ML fits to the 45-month *Fermi*-LAT data for three galaxy clusters: Coma, Fornax and Virgo. We fit models which, in addition to point sources and galactic and extragalactic backgrounds, include emission due to DM annihilation and CR. For the former, we assume both a point source and the theoretically predicted extended distribution of gamma-rays in three generic annihilation channels, the $b\bar{b}$, $\mu^+\mu^-$ and $\tau^+\tau^-$ channels. When searching for a DM signal, we experiment with different treatments of the CR component. In the traditional *Fermi* analysis, the extragalactic background (EG) is assumed to be a smooth component. In this work we have also investigated a more realistic EG model where a fraction of the EG emission comes from a population of undetected point sources.

Performing a standard likelihood analysis we obtain the following results.

(i) In all three clusters and for the four different treatments of CR we have implemented, no significant detection of DM emission is obtained. We set upper limits on the flux and cross-section of DM annihilation in the three clusters we have investigated. Uncertainties in the CR component have only a mild effect on the upper limits: for the different CR models, the DM upper limit constraints agree to within a factor of 2.

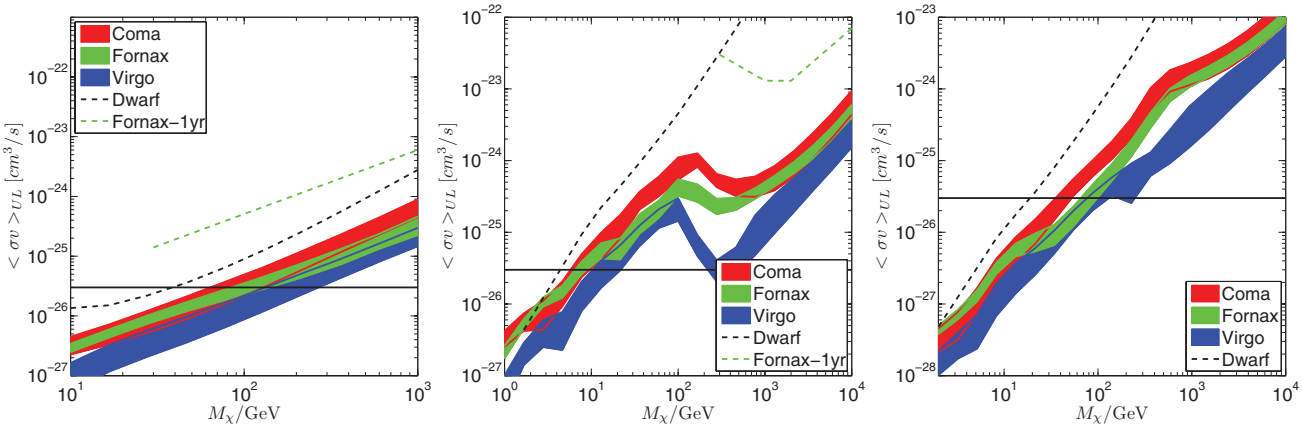

Figure 10. Upper limits for the DM annihilation cross-section in the $b\bar{b}$ (left), $\mu^+\mu^-$ (middle) and $\tau^+\tau^-$ (right) channels, after including the effect of undetected point sources. The line styles are as in Fig. 6, but only the EXT results are shown. Note that the lower bounds of each band are still determined by the results without including undetected point sources in the analysis.

Models in which the DM annihilation emission has the extended profile predicted by cosmological simulations (Gao et al. 2011) have higher flux upper limits than models in which this emission is assumed to be a point source. Due to the large luminosity enhancement, of the order of 1000, by emission from subhaloes, the upper limits on the annihilation cross-section for extended models are at least 100 times lower than those for point source models. Our cross-section constraints are much tighter than those from an analysis of clusters using the 11-month data (Ackermann et al. 2010), mostly because we take into account the effect of subhaloes. Our constraints are also tighter than those from a joint analysis of Milky Way dwarf galaxies (Geringer-Sameth & Koushiappas 2011; Ackermann et al. 2011).

Our new limits exclude the thermal cross-section for $M_\chi \lesssim 100$ GeV for $b\bar{b}$ and $\tau^+\tau^-$ final states, and for $M_\chi \lesssim 10$ GeV for $\mu^+\mu^-$ final states. We note that the annihilation cross-section in DM haloes need not be the standard thermal cross-section of supersymmetric models. In cases where the cross-section is velocity dependent, for example, through p-wave contributions at freeze-out (see e.g. Jungman et al. 1996), one can easily have a different average cross-section. We emphasize that there is still a large uncertainty in our adopted annihilation profile, which depends on a significant extrapolation of the resolved subhalo population by more than 10 orders of magnitude in mass. Taking this into account, the thermal cross-section, however, could still be reconciled with the data by assuming a larger cutoff mass in the WIMP power spectrum, thus reducing the contribution from subhaloes and hence the J factor. Since the total enhancement from subhalo emission scales as $b \propto M_{\rm cut}^{-0.226}$ (Springel et al. 2008), a cutoff mass of $10^{-4}\,{\rm M}_\odot$, rather than our assumed $10^{-6}\,{\rm M}_\odot$, would be sufficient to increase the cross-section limits by a factor of 3.

(ii) Assuming no DM annihilation radiation, the gamma-ray data for Coma and Virgo already set significant constraints on the CR level. For Virgo, the data are consistent with the predictions of the analytic CR model proposed by Pinzke & Pfrommer (2010) and Pinzke et al. (2011), while for Coma, the data place an upper limit that is a factor of 2 below the analytical prediction, indicating either an uncertainty in the model parameters such as halo mass, gas density and maximum shock injection efficiency, $\zeta_{p,\rm max}$, or a peculiarity of the CR emission in Coma. If attributed to $\zeta_{p,\rm max}$, the upper limit on the normalization parameter, $\alpha_{\rm CR}$, translates into an upper limit on $\zeta_{p,\rm max}$ of 0.3, assuming a linear form for $g(\zeta_{p,\rm max})$. This is consistent with the estimates obtained independently by Zimmer et al. (2011) for Coma using *Fermi* data and by the Aleksić et al. (2012) for the Persus cluster using Major Atmospheric Gamma-ray Imaging Cherenkov Telescopes (MAGIC) observations. If interpreted as an error in the halo mass, a reduction in mass by a factor of 1.6 is required to reconcile the model with the upper limits, assuming a simple CR luminosity scaling relation, $L_\gamma \propto M_{200}^{1.46}$ (Pinzke & Pfrommer 2010), or by a factor of 4.3 according to equation (D1) in the case when the gas density profile is fixed from X-ray observations. For Fornax, the zero significance of a CR component is consistent with the low level predicted by the model.

(iii) Five new point sources with TS > 25 in Virgo and Fornax have been detected in the 45-month data. Ignoring these new point sources results in a $\sim 5\sigma$ detection for a DM component in Virgo, in contrast to a $\sim 3\sigma$ detection when these point sources are taken into account.

In addition to the standard likelihood analysis, we have also investigated a model in which the EG component includes a population of undetected point sources whose number–flux relation extrapolates smoothly that of the detected sources. Using Monte Carlo simulations, we find that the standard *Fermi* likelihood analysis could overestimate the TS of extended emission by a factor of 2−3 and underestimate the upper limits by up to 70 per cent. Adopting this more realistic EG model yields slightly looser upper limits, but does not quantitatively change any of the above conclusions. Still, it should be kept in mind that these corrections are derived from simulations assuming a particular distribution for the point source population. It is too computationally expensive to explore the parameter space of point source populations with Monte Carlo simulations. A more detailed and more general analytical study of the effect of undetected point sources will be presented elsewhere (Han et al., in preparation).

In our analysis we have allowed the parameters of 2FGL point sources lying within the cluster virial radius to vary. This accounts for possible corrections to the 2FGL parameters in the presence of a DM or a CR component, while also avoiding the risk of refitting sources lying near the boundary of the data region with less accuracy. The parameters of highly variable sources are also kept free since the 2FGL parameters for these sources would be the average during a 2-yr period whereas here we have 45 months of data. However, we also tried keeping all the point sources fixed or allowing

the parameters of all the point sources within the data region to vary during the fitting. We find that this freedom in the treatment of the point sources has little impact on the DM model fits.

The cluster annihilation luminosity scales roughly linearly with halo mass, with the shape of the profile being almost independent of halo mass or concentration when expressed in terms of the normalized radius r/R_{200}. We investigate the effect of mass uncertainties in Appendix E. We have also checked that the different energy cuts assumed in our analysis and in that of Huang et al. (2012) have no effect on the derived upper limits. We are able to reproduce the upper limits on the annihilation cross-section of Huang et al. (2012) for the test case of the Fornax cluster with 3-yr data, after adopting the same IRF and correcting for slightly different assumed subhalo contributions.

The CR model used in this analysis is still subject to improvement. This model is derived from simulations which, unavoidably, make simplifying assumptions. For example, the simulations only consider advective transport of CR by turbulent gas motions, but there are other processes such as CR diffusion and streaming which may flatten the CR profiles (Enßlin et al. 2011). In particular, if the CR diffusion is momentum dependent, this will entangle the spectral and spatial profile of CR and modify the morphology as well as the spectrum of the CR emission, thus invalidating our basic assumption that $\alpha_{\rm CR}$ is the only free parameter. There could also be CR injected from AGN which are not accounted for in the current model.

Although we have not detected DM annihilation emission in our small cluster sample, the signal-to-noise ratio can potentially be enhanced by stacking many clusters. Such an analysis was recently carried out by Huang et al. (2012), but the signal-to-noise ratio was degraded because of their assumption of an NFW annihilation profile. These authors considered an extended subhalo-dominated annihilation profile but only for individual clusters, not for the stack. Their stacked analysis placed looser constraints on DM annihilation emission than their analysis of individual clusters, presumably because the use of an inappropriate theoretical profile resulted in the different clusters yielding inconsistent results. Thus, it is clearly worth repeating the joint analysis with the 'correct' subhalo-dominated profile. It is also tempting to extend the search for DM annihilation using multiwavelength data, from the radio to very high energy gamma-rays and even in the neutrino channel (Dasgupta & Laha 2012), where different systematics are expected for different bands.

ACKNOWLEDGMENTS

We thank Shaun Cole, Jie Liu, Yu Gao, John Lucey, Anders Pinzke, Christoff Pfrommer, Dan Hooper, Neal Weiner, Douglas Finkbeiner, Gregory Dobbler, Louie Strigari, Christoph Weniger, Savvas Koushiappas and Fabio Zandanel for helpful discussions. JXH acknowledges the support on software issues from Tesla Jeltema and the Fermi science support team, especially Elizabeth C. Ferrara, Jeremy S. Perkins, Dave Davis and Robin Corbet. JXH is supported by the European Commissions Framework Programme 7, through the Marie Curie Initial Training Network Cosmo-Comp (PITNGA-2009-238356), and partially supported by NSFC (10878001, 11033006, 11121062) and by the CAS/SAFEA International Partnership Programme for Creative Research Teams (KJCX2-YW-T23). CSF acknowledges a Royal Society Wolfson research merit award and an ERC Advanced Investigator grant. The calculations for this work were performed on the ICC Cosmology Machine, which is part of the DiRAC Facility jointly funded by STFC, the Large Facilities Capital Fund of BIS and Durham University. This work was supported in part by an STFC rolling grant to the ICC. The work of DM is supported in part from the SCOPES project IZ73Z0 128040 of Swiss National Science Foundation, grant No CM-203-2012 for young scientists of National Academy of Sciences of Ukraine, Cosmomicrophysics programme of the National Academy of Sciences of Ukraine and by the State Programme of Implementation of Grid Technology in Ukraine. We thank the *Fermi* team for making the LAT data publicly available. This research has made use of the NASA/IPAC Extragalactic Database (NED) which is operated by the Jet Propulsion Laboratory, California Institute of Technology, under contract with the National Aeronautics and Space Administration.

REFERENCES

Aalseth C. E. et al., 2011a, Phys. Rev. Lett., 106, 131301
Aalseth C. E. et al., 2011b, Phys. Rev. Lett., 107, 141301
Abazajian K. N., Kaplinghat M., 2012, Phys. Rev. D, 86, 083511
Abdo A. A. et al., 2009, ApJ, 707, 55
Abdo A. A. et al., 2010, ApJ, 720, 435
Ackermann M. et al., 2010, J. Cosmol. Astropart. Phys., 5, 25
Ackermann M. et al. (The Fermi-LAT Collaboration), 2011, Phys. Rev. Lett., 107, 241302
Ahmed Z. et al., 2011, Phys. Rev. Lett., 106, 131302
Aleksić J. et al. (MAGIC Collaboration), 2012, A&A, 541, A99
Angloher G. et al., 2012, Eur. Phys. J. C, 72, 1971
Aprile E. et al., 2011, Phys. Rev. Lett., 107, 131302
Baxter E. J., Dodelson S., 2011, Phys. Rev. D, 83, 123516
Bernabei R. et al., 2010, Eur. Phys. J. C, 67, 39
Bertone G., Hooper D., Silk J., 2004, Phys. Rep., 405, 279
Böhringer H., Briel U. G., Schwarz R. A., Voges W., Hartner G., Trümper J., 1994, Nat, 368, 828
Boyarsky A., Malyshev D., Ruchayskiy O., 2011, Phys. Lett. B, 705, 165
Boyarsky A., Malyshev D., Ruchayskiy O., 2012, preprint (arXiv:1205.4700)
Bringmann T., Huang X., Ibarra A., Vogl S., Weniger C., 2012, J. Cosmol. Astropart. Phys., 7, 54
Ciafaloni P., Comelli D., Riotto A., Sala F., Strumia A., Urbano A., 2011, J. Cosmol. Astropart. Phys., 3, 19
Cirelli M. et al., 2011, J. Cosmol. Astropart. Phys., 3, 51
Collar J. I., 2011a, preprint (arXiv:1103.3481)
Collar J. I., 2011b, preprint (arXiv:1106.0653)
Dasgupta B., Laha R., 2012, preprint (arXiv:1206.1322)
Diemand J., Kuhlen M., Madau P., 2007, ApJ, 657, 262
Duffy A. R., Schaye J., Kay S. T., Dalla Vecchia C., 2008, MNRAS, 390, L64
Enßlin T., Pfrommer C., Miniati F., Subramanian K., 2011, A&A, 527, A99
Finkbeiner D. P., 2004, Astrophysics, preprint (astro-ph/0409027)
Fouqué P., Solanes J. M., Sanchis T., Balkowski C., 2001, A&A, 375, 770
Gao L., Frenk C. S., Jenkins A., Springel V., White S. D. M., 2012, MNRAS, 419, 1721
Geringer-Sameth A., Koushiappas S. M., 2011, Phys. Rev. Lett., 107, 241303
Gondolo P., Silk J., 1999, Phys. Rev. Lett., 83, 1719
Han J., Frenk C. S., Eke V. R., Gao L., White S. D. M., 2012, preprint (arXiv:1201.1003)
Hoffman G. L., Olson D. W., Salpeter E. E., 1980, ApJ, 242, 861
Hooper D., 2012, preprint (arXiv:1201.1303)
Hooper D., Goodenough L., 2011, Phys. Lett. B, 697, 412
Hooper D., Linden T., 2011a, Phys. Rev. D, 83, 083517
Hooper D., Linden T., 2011b, Phys. Rev. D, 84, 123005
Hooper D., Finkbeiner D. P., Dobler G., 2007, Phys. Rev. D, 76, 083012
Huang X., Vertongen G., Weniger C., 2012, J. Cosmol. Astropart. Phys., 1, 42
Jeltema T. E., Kehayias J., Profumo S., 2009, Phys. Rev. D, 80, 023005
Jungman G., Kamionkowski M., Griest K., 1996, Phys. Rep., 267, 195
Karachentsev I. D., Nasonova O. G., 2010, MNRAS, 405, 1075

Linden T., Hooper D., Yusef-Zadeh F., 2011, ApJ, 741, 95
Macías-Ramírez O., Gordon C., Brown A. M., Adams J., 2012, Phys. Rev. D, 86, 076004
Mattox J. R. et al., 1996, ApJ, 461, 396
Nolan P. L. et al. (The Fermi-LAT Collaboration), 2012, ApJS, 199, 31
Pinzke A., Pfrommer C., 2010, MNRAS, 409, 449
Pinzke A., Pfrommer C., Bergström L., 2011, Phys. Rev. D, 84, 123509
Schindler S., Binggeli B., Böhringer H., 1999, A&A, 343, 420
Smith S., 1936, ApJ, 83, 23
Springel V. et al., 2008, Nat, 456, 73
Su M., Finkbeiner D. P., 2012, preprint (arXiv:1206.1616)
Tempel E., Hektor A., Raidal M., 2012, J. Cosmol. Astropart. Phys., 9, 32
Tonry J. L., Blakeslee J. P., Ajhar E. A., Dressler A., 2000, ApJ, 530, 625
Tully R. B., Shaya E. J., 1984, ApJ, 281, 31
Urban O., Werner N., Simionescu A., Allen S. W., Böhringer H., 2011, MNRAS, 414, 2101
Vitale V., Morselli A., for the Fermi/LAT Collaboration, 2009, preprint (arXiv:0912.3828)
Weniger C., 2012, J. Cosmol. Astropart. Phys., 8, 7
Zaharijas G., Cuoco A., Yang Z., Conrad J., 2010, preprint (arXiv:1012.0588)
Zimmer S., Conrad J., for the Fermi-LAT Collaboration, Pinzke A., 2011, preprint (arXiv:1110.6863)

APPENDIX A: DETECTION OF NEW POINT SOURCES

We model the new point sources assuming power-law spectra. For a given pixel, we calculate the TS value for an assumed new point source centred on that pixel. The TS calculation is performed using the binned method in the `pyLikelihood` tool, with a null model which includes the GAL and EG components and all the 2FGL sources within 15° of each cluster, but with the parameters of the 2FGL sources fixed. Around each cluster, we carry out a first scan of all the pixels within the cluster virial radius (and within 4° around Coma) using a pixel size of 0.2.

Regions with a peak TS > 16 are identified as potential locations of new point sources. We then scan each potential point source region using 10 times smaller pixels. The calculated TS map is then interpolated with cubic splines down to 0.002 pixel^{-1}. The value and location of the TS peak are taken as the TS and position for a new point source, if the peak TS > 25. In case several peaks are clustered, we first extract the primary TS peak, then scan for lower TS peaks by including the newly detected sources into the null model. In our sample, no secondary peaks survive this iterative examination to be identified as new point sources.

The new point sources are listed in Table A1, and plotted in Figs 1 and C1. Sources in Virgo and Fornax are prefixed by 'V' and 'F' in their names, respectively. None of these new sources show significant variability when binned over monthly scale. The last column of Table A1 shows possible associations of astrophysical sources with these new detections, which are found to lie within the 2σ confidence region of the detections.

APPENDIX B: MONTE CARLO SIMULATION OF UNDETECTED POINT SOURCE POPULATIONS

To model the undetected population we adopt the following model based on the results of Abdo et al. (2010). Each point source is assumed to have a power-law spectrum defined by two parameters: flux and spectral index. The spectral index distribution is modelled as a Gaussian of mean $\mu = 2.36$ and $\sigma = 0.27$. The flux and spectral index are assumed to be independent. The differential number density of undetected point sources is assumed to be given by

$$\frac{\mathrm{d}N}{\mathrm{d}S\mathrm{d}\Omega} = A\left(\frac{S}{S_b}\right)^{-\beta}. \tag{B1}$$

We adopt $S_b = 6.6 \times 10^{-8}$ ph cm^{-2} s^{-1}, $\beta = 1.58$ and $A = 4.1 \times 10^8$ cm^2 s Sr^{-1}, as derived from table 4 of Abdo et al. (2010). Since the total number of point sources diverges for $\beta > 1$, we cut off the flux distribution at $S_{\min} = 1 \times 10^{-11}$ ph cm^{-2} s^{-1}. Due to the dependence of the detection efficiency on flux and spectral shape, there is no obvious cutoff in the maximum flux of undetected sources. We take $S_{\max} = 1 \times 10^{-8}$ ph cm^{-2} s^{-1} as the detection threshold which corresponds to a detection completeness of ∼50 per cent, comparing 2FGL source counts and the model. This implies an undetected point source flux of 14 per cent of the standard EG background, consistent with the results of Abdo et al. (2010). The synthetic spectrum of these undetected point sources is then subtracted from the standard EG template to yield a residual EG template for the simulation.

We perform 750 independent realizations of the 15° Virgo region in the presence of undetected point sources. For each realization, we generate mock data in the following steps.

(i) Generate a Poisson random number for the total number of undetected point sources within 15°.

(ii) For each point source, generate a random spectral index and a random flux according to the distributions specified above. Also, generate random coordinates for the point source according to a uniform distribution on the sky.

(iii) Feed these point sources and the 2FGL point sources within 15°, as well as the GAL and remaining EG components, to `gtobssim`.

The standard likelihood analysis is then applied to the simulated data without including any of the randomly generated point sources in the model. Here we only consider the CR-only and the DM-only models. In Fig. B1 we show the cumulative probability distribution of TS values. Simple scaled versions of the standard χ^2(TS)/2 distributions can roughly describe the TS distribution and provide the simplest way to convert the fitted TS to the standard χ^2-distributed TS.

Table A1. Newly detected point sources.

Name	TS	RA (°)	Dec. (°)	Flux (10^{-9} ph cm^{-2} s^{-1})	Spectral index[a]	Separation (°)[b]	Possible association
V1	32.5	190.920	16.194	5.9 ± 1.4	-2.3 ± 0.2	4.96	LBQS 1241+1624
V2	31.8	185.698	11.116	3.7 ± 1.0	-2.0 ± 0.2	2.31	[VV2006] J122307.2+110038
V3	31.6	184.066	9.456	2.3 ± 0.8	-1.9 ± 0.2	4.58	2MASX J12160619+0929096
V4	30.5	185.894	8.286	1.6 ± 0.7	-1.8 ± 0.2	4.42	SDSS J122321.38+081435.2
F1	26.3	58.300	−36.386	0.9 ± 0.6	-1.7 ± 0.3	3.17	[VV98b] J035305.1−362308

[a]Photon spectral index β for $\mathrm{d}N/\mathrm{d}E \propto E^{\beta}$.
[b]Distance to cluster centre.

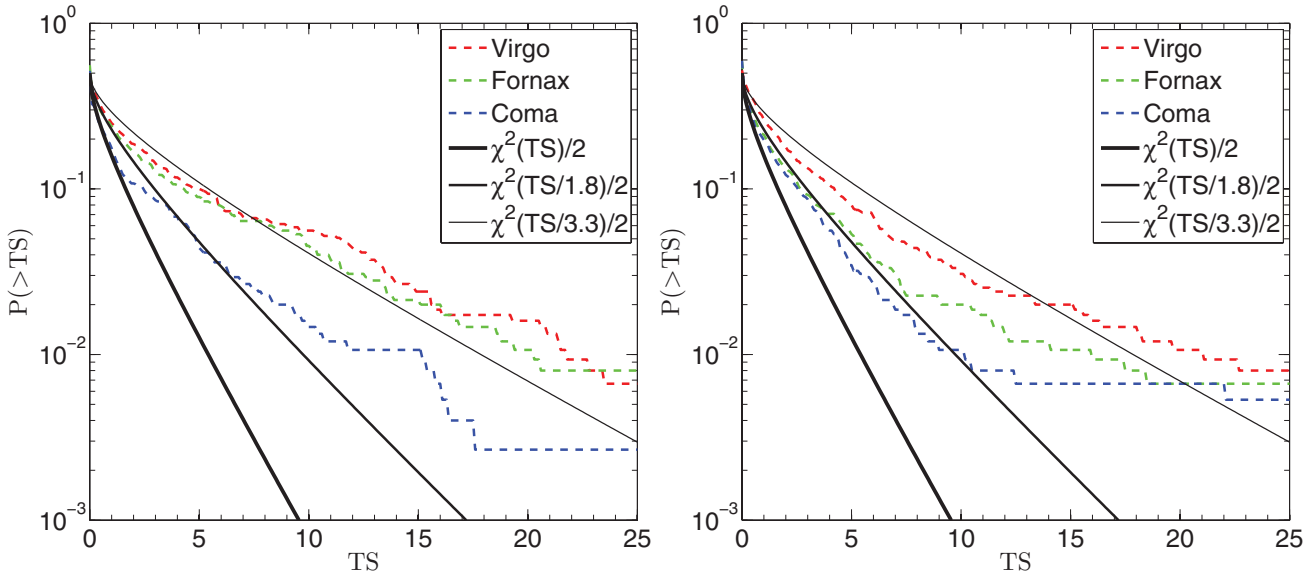

Figure B1. Distribution of TS from simulated data which include a population of undetected point sources. Left: the distribution of TS for DM-only models, where the DM particle mass is taken to be ∼30 GeV and the DM follows the EXT cluster profile. Right: the distribution of TS for CR-only models. In each panel the dashed lines show the distribution extracted from the simulations for three cluster models, and the solid lines show a rescaled version of the standard cumulative χ^2 distribution.

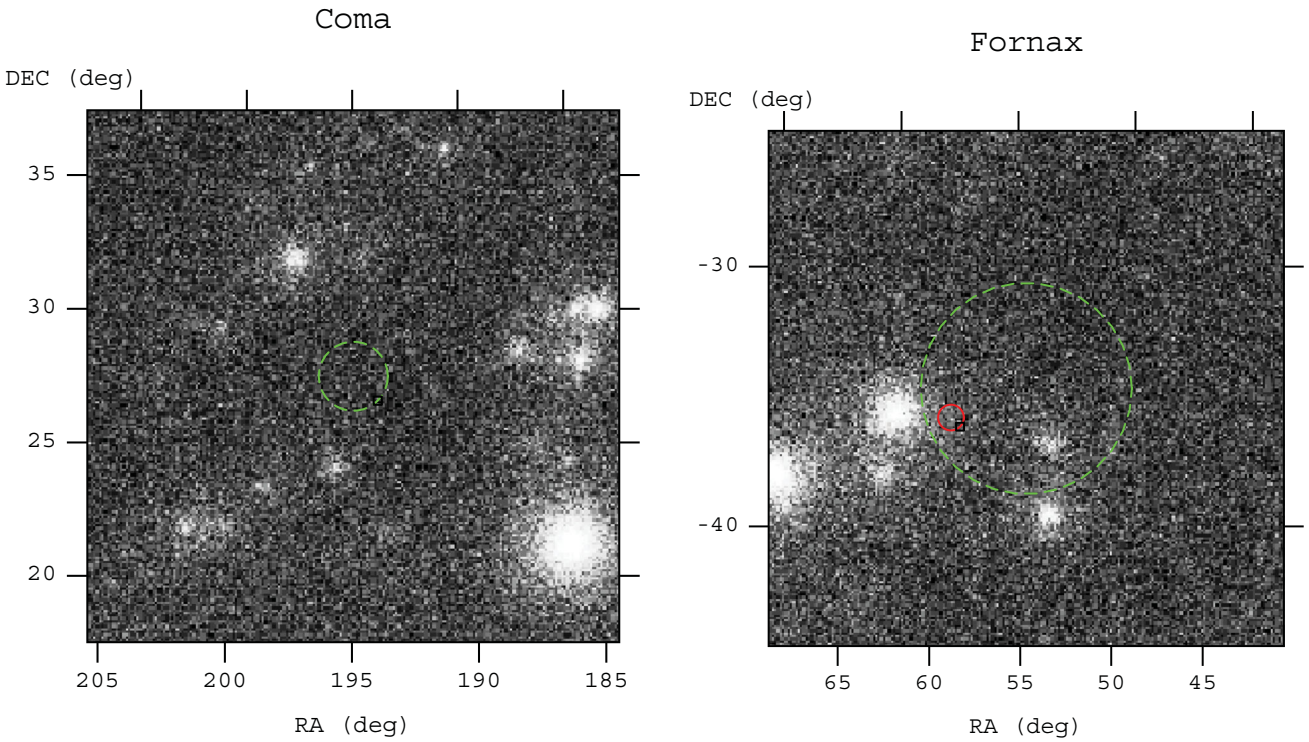

Figure C1. Integrated gamma-ray images in the Coma (left) and Fornax (right) cluster regions. The green dashed circle marks the virial radius of the cluster. Each image covers 20 × 20 deg^2 with a pixel size of 0.°1, constructed from the 3-yr *Fermi*-LAT data applying the data cuts described in the main text. The small solid circle in Fornax marks the position of a newly detected point source.

APPENDIX C: GAMMA-RAY IMAGES FOR COMA AND FORNAX

In this appendix we show gamma-ray images for the Coma and Fornax cluster regions. The corresponding image for Virgo is shown in Fig. C1.

APPENDIX D: SEMI-ANALYTIC FORMULA FOR THE CR-INDUCED GAMMA-RAY EMISSION

Here we summarize the relevant equations for calculating the CR-induced gamma-ray emission in galaxy clusters as derived by Pinzke

& Pfrommer (2010) and Pinzke et al. (2011). The CR-induced photon source function from pion decay can be decomposed as

$$\frac{\mathrm{d}N_\gamma}{\mathrm{d}t\ \mathrm{d}V\ \mathrm{d}E} = A(r)s(E).$$

The spatial part is given by

$$A(r) = \left((C_{200} - C_{\rm centre}) \left(1 + \left(\frac{r}{R_{\rm trans}} \right)^{-\beta} \right)^{-1} + C_{\rm centre} \right) \rho_{\rm gas}(r)^2, \quad \text{(D1)}$$

with

$$C_{\rm centre} = 5 \times 10^{-7} \quad \text{(D2)}$$

$$C_{200} = 1.7 \times 10^{-7} \times \left(M_{200}/10^{15}\,\mathrm{M}_\odot \right)^{0.51} \quad \text{(D3)}$$

$$R_{\rm trans} = 0.021 R_{200} \times \left(M_{200}/10^{15}\,\mathrm{M}_\odot \right)^{0.39} \quad \text{(D4)}$$

$$\beta = 1.04 \times \left(M_{200}/10^{15}\,\mathrm{M}_\odot \right)^{0.15}. \quad \text{(D5)}$$

The spectrum is given as

$$s(E) = g(\zeta_{p,\rm max}) D_\gamma(E_\gamma, E_{\gamma,\rm break}) \frac{16}{3 m_{\rm p}^3 c} \times \sum_{i=1}^{3} \frac{\sigma_{pp,i}}{\alpha_i} \left(\frac{m_{\rm p}}{2 m_{\pi^0}} \right)^{\alpha_i} \Delta_i \left[\left(\frac{2E_\gamma}{m_{\pi^0} c^2} \right)^{\delta_i} + \left(\frac{2E_\gamma}{m_{\pi^0} c^2} \right)^{-\delta_i} \right]^{-\frac{\alpha_i}{\delta_i}}, \quad \text{(D6)}$$

with $\Delta = (0.767, 0.143, 0.0975)$, $\alpha = (2.55, 2.3, 2.15)$, $\delta_i \simeq 0.14\alpha_i^{-1}.6 + 0.44$. Here $m_{\rm p}$ is the proton mass, m_{π^0} the neutral pion mass and c the speed of light. The maximum shock acceleration efficiency is chosen to be $\zeta_{p,\rm max} = 0.5$ so that $g(\zeta_{p,\rm max}) = 1$. The term $D_\gamma(E_\gamma, E_{\gamma,\rm break})$ describes the diffusive CR losses due to escaping protons as

$$D_\gamma(E_\gamma, E_{\gamma,\rm break}) = \left[1 + \left(\frac{E_\gamma}{E_{\gamma,\rm break}} \right)^3 \right]^{-1/9}. \quad \text{(D7)}$$

The proton cutoff energy is

$$E_{p,\rm break} \approx \frac{10^8}{8}\,\mathrm{GeV} \left(\frac{R_{200}}{1.5\,\mathrm{Mpc}} \right)^6. \quad \text{(D8)}$$

The energy $E_{p,\rm break}$ is related to the photon cutoff energy, $E_{\gamma,\rm break}$, through the momentum relation $P_\gamma \approx \frac{P_{\rm p}}{8}$. The effective cross-section for proton–proton interactions is given by

$$\sigma_{{\rm pp},i} \simeq 32(0.96 + \mathrm{e}^{4.42 - 2.4\alpha_i})\mathrm{Mbarn}. \quad \text{(D9)}$$

The gas density is fitted with multiple beta profiles:

$$\rho_{\rm gas} = \frac{m_{\rm p}}{X_{\rm H} X_{\rm e}} \left\{ \sum_i n_i^2(0) \left[1 + \left(\frac{r}{r_{c,i}} \right)^2 \right]^{-3\beta_i} \right\}^{1/2}, \quad \text{(D10)}$$

where $X_{\rm H} = 0.76$ is the primordial hydrogen mass fraction and $X_{\rm e} = 1.157$ is the ratio of electron and hydrogen number densities in the fully ionized intracluster medium, with parameter values for $n_i(0)$, $r_{c,i}$ and β_i listed in table 6 of Pinzke et al. (2011).

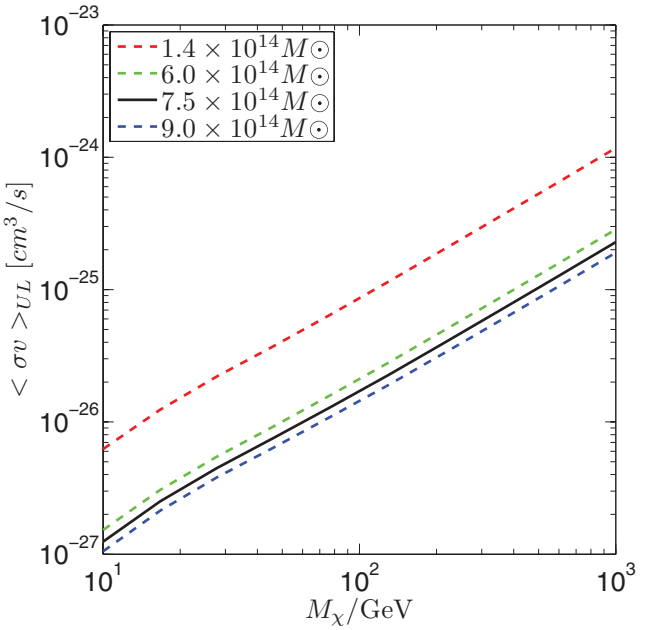

Figure E1. Upper limits on the cross-section for DM annihilating into the $b\bar{b}$ channel in the no-CR model. The different lines correspond to different adopted values for the mass of the DM halo of the Virgo cluster, as labelled. No allowance for undetected point sources has been made in this figure.

APPENDIX E: EFFECT OF MASS UNCERTAINTIES IN VIRGO

We adopt a virial mass for Virgo of $7.5 \pm 1.5 \times 10^{14}\,\mathrm{M}_\odot$, as estimated by Tully & Shaya (1984), from an analysis of the infall pattern of galaxies around Virgo. This value is consistent with other dynamical measurements (Smith 1936; Hoffman, Olson & Salpeter 1980; Tonry et al. 2000; Fouqué et al. 2001; Karachentsev & Nasonova 2010). Mass estimates from X-ray gas modelling tend to give somewhat lower values (Böhringer et al. 1994; Schindler, Binggeli & Böhringer 1999; Urban et al. 2011). Thus, in addition to our adopted mass uncertainty from Tully & Shaya (1984), as an extreme case, we consider also a value of $1.4 \times 10^{14}\,\mathrm{M}_\odot$, obtained by scaling the X-ray estimate to the virial radius (Urban et al. 2011). In Fig. E1 we show the effect of adopting these different masses on the upper limits for DM annihilation in the $b\bar{b}$ channel. Since the flux upper limit is insensitive to slight changes in the profile shape and thus in the mass, while the luminosity (or integrated J factor) scales linearly with mass, the cross-section upper limits are expected to be roughly inversely proportional to mass. This is indeed the case in Fig. E1, where $\langle \sigma v \rangle_{\rm UL} \propto M_{200}^{-0.9}$.

This paper has been typeset from a TEX/LATEX file prepared by the author.